Cite this article as:
F.N. Ponzio, A. Tamburini, A. Cipollina, G. Micale, Ciofalo, Experimental and computational investigation of heat transfer in channesl filled by woven spacers, *International Journal of Heat and Mass Transfer*, 104 (2017) 163-177.
doi: 10.1016/j.ijheatmasstransfer.2016.08.023

EXPERIMENTAL AND COMPUTATIONAL INVESTIGATION OF HEAT TRANSFER IN CHANNELS FILLED BY WOVEN SPACERS

F. N. Ponzio, A. Tamburini*, A. Cipollina, G. Micale, M. Ciofalo

Dipartimento di Ingegneria Chimica, Gestionale, Informatica, Meccanica
Università degli Studi di Palermo, Viale delle Scienze, 90128 Palermo, Italy

ABSTRACT

Models of woven-type spacer-filled channels were investigated by Computational Fluid Dynamics (CFD) and parallel experiments in order to characterize the performance of Membrane Distillation (MD) modules. The case of overlapped spacers was analysed in a companion paper.

Experiments were based on a non-intrusive technique using Thermochromic Liquid Crystals (TLC) and digital image processing, and provided the distribution of the local convective heat transfer coefficient on a thermally active wall. CFD simulations ranged from steady-state conditions to unsteady and early turbulent flow, covering a Reynolds number interval of great practical interest in real MD applications. A specific spacer aspect ratio (pitch-to-channel height ratio of 2) and two different spacer orientations with respect to the main flow (0° and 45°) were considered.

Among the existing studies on spacer-filled channels, this is one of the first dealing with *woven* spacers, and one of the very few in which *local* experimental and computational heat transfer results are compared. Results suggest a convenience in adopting the 45° orientation for applications that can be operated at very low Reynolds numbers, since convenience decreases as the Reynolds number increases.

Keywords: *Membrane Distillation; Woven Spacer; Thermochromic Liquid Crystals; Digital Image Processing; Computational Fluid Dynamics*

* Corresponding author; email alessandro.tamburini@unipa.it, tel. +39 091 23863780

1 INTRODUCTION

1.1 Spacer-filled channels

Several membrane-based processes, e.g. Membrane Distillation [1], Reverse Osmosis [2] and Reverse Electrodialysis [3], involve flow and heat or mass transfer in spacer-filled plane channels. Spacers serve the double purpose of maintaining the appropriate distance between the channel walls and promoting mixing, thus reducing polarization and increasing transfer rates [4].

Applications differ in size (channel height from 10^{-4} to 10^{-2} m), flow regime (from creeping to turbulent) and quantity being transferred (heat, water, ions etc.), but involve comparable spacer geometries. For example, Figure 1 reports examples taken from three families of net spacers (extruded, overlapped, woven) which have been paid particular attention in the literature. More complex spacer shapes have also been proposed [5, 6, 7].

Overlapped wire spacers have been the subject of a previous study by our research group [8]. Recently obtained experimental and computational results for woven spacers are presented here.

1.2 Literature review

Temperature polarization may severely impair the performance of MD modules [9]. Spacers interposed between the walls of a plane channel promote mixing and reduce polarization, thus enhancing heat or mass transport and reducing fouling issues [4, 10]. Unfortunately, they also cause pressure drop to increase [11]. Thus, much research effort has been devoted to the search for spacer configurations offering a compromise between heat or mass transfer and hydraulic losses [8, 11-15].

Different applications of spacer-filled channels are characterized by different spatial scales and flow rates, and thus the flow regimes expected are different. For example, low Reynolds number steady-state flow is typical in Reverse Electrodialysis, whereas unsteady and turbulent flow may occur in Membrane Distillation. It should be kept in mind that, in the complex flow passages

created by spacers, the base steady state flow may well lose stability at critical Reynolds numbers of a few hundred, much lower than those holding in plane channels and other simple ducts [8, 16].

The literature is poor of results for woven spacers. What can be said is that woven spacers, either of the simple type in Figure 1(c) or more complex, seem to provide better heat / mass transfer performances than overlapped spacers in MD and other membrane processes [17]. Unfortunately, also pressure drops are significantly higher [18].

In recent years, Computational Fluid Dynamics (CFD) has been increasingly employed to investigate flow field and transport features in spacer-filled channels. Once properly validated against experimental data, CFD provides valuable local information on both existing spacers and novel ones. While most CFD studies have limited the analysis to the *steady* regime [10, 19-23], a few have been devoted to the CFD simulation of *unsteady* flows. For example, Koutsou *et al*. [16] performed Direct Numerical Simulations (DNS) highlighting that unsteadiness may occur even at low Reynolds numbers; Mahdavifar *et al*. [24] employed DNS to investigate the effects of the spacer-to-wall clearance on the flow field; and Tamburini *et al*. [8] simulated early turbulent flow in channels filled with overlapped-type spacers using DNS. At high Reynolds number, DNS can become too computationally expensive, and the use of a turbulence model may be more suitable. For example, Shakaib *et al*. [25] employed the Spalart-Allmaras model (based on a single transport equation for the turbulent viscosity) to predict temperature polarization in membrane distillation modules.

1.3 The issue of CFD validation

The problem of CFD results validation in geometrically or physically complex problems deserves a brief discussion. Steady-state, laminar flow simulations, provided mathematical consistency and grid-independence are demonstrated, do not really require being validated against experimental data, since they are potentially more accurate than any possible experiment and, at most, should be

compared with analytical solutions (if any exist) or with previous numerical simulations of demonstrated high accuracy.

Rather, the real purpose of a comparison between CFD predictions and experimental results should be to check to what extent the complexity of the actual physical system is sufficiently reflected in the computational model, i.e. to quantify the influence of assumptions like neglecting minor geometrical irregularities or describing the actual flow and thermal boundary conditions as canonical (Dirichlet, Neumann or Cauchy) ones.

In this respect, *local* data, e.g. the 3-D flow and thermal fields and the distribution of the heat transfer coefficient on a thermally active wall, are more useful than *global* experimental results like the friction coefficient and the mean heat transfer coefficient. We have recently applied an experimental technique, based on thermochromic liquid crystals and digital image processing, which provides local distributions of wall temperature and heat transfer coefficient [8, 15, 26-28]. Of course, local data can also be processed to extract global (average) quantities.

1.4 Statement of the problem

In this study, a woven spacer is assumed to consist of two arrays of identical cylindrical wires, or filaments, of diameter d, arranged orthogonally in a woven fashion at a right angle with pitch l, see Figure 2(a). A further parameter is the angle θ formed by either filament array with the main flow direction (more general configurations might be obtained by letting the diameters of the two filament arrays differ, or the included angle be other than 90°). Both in the experiments and in the numerical simulations, heat transfer will be assumed to occur only from one of the walls (top wall, representing the fluid-membrane interface), the opposite one (bottom wall) being adiabatic. Of course, this is only one of the possible set of thermal boundary conditions which have been proposed or tested in real Membrane Distillation plant, and was chosen here for the relative ease by which it can be realized in the experiments (as opposed, for example, to bilateral heat transfer).

Unlike in overlapped spacers [8], a periodic unit cell, to be used both as the computational domain in the numerical simulations and as the reference region in the experiments, must include not a single square of the filament mesh, but a larger portion of it; the choice adopted here, which is only one of several possible alternatives, is shown in Figure 2(b). Here the cell volume is twice that of a single mesh square.

The quantities measured or computed are the heat transfer coefficient at the thermally active wall (mean value *and* distribution) and the pressure drop as functions of the parameters d, l, θ and of the flow rate. In dimensionless terms, the problem reduces to determining the Nusselt number (mean value and distribution on the wall) and the friction coefficient as functions of l/d, θ and Re (Reynolds number).

In all spacers, the flow attack angle θ is responsible for changes in flow direction and flow pattern which affect polarization and heat transfer [25] and thus deserves a particular attention. Results will be presented here for two flow attack angles, 0° and 45°. Due to the symmetries of the problem, the 90° orientations is equivalent to the 0° one; also, it is sufficient to investigate the range θ=0° through 45° since, apart from reflections, the same flow and thermal fields repeat themselves periodically for larger angles.

The pitch-to-channel height ratio is kept fixed at 2 (pitch-to-filament diameter ratio = 4). This, too, may be an important parameter and its influence is currently being investigated by our group.

As in our previous paper [8], dimensionless quantities are defined with reference to the corresponding void (spacerless) configuration, i.e. to a plane channel having height H and thus hydraulic diameter D_h=2H. Coherently, the bulk Reynolds number is

$$\mathrm{Re} = U \cdot 2H/\nu \qquad (1)$$

in which $U = Q/(WH)$ is the mean "void channel" streamwise velocity, being Q the volume flow rate and W the channel's spanwise extent (in the experiments, $H \approx 0.01$ m and $W \approx 0.22$ m). This scaling is preferable to that based on the actual hydraulic diameter and mean velocity of each

specific case, and makes comparisons between different configurations more meaningful. The friction velocity Reynolds number Re_τ is defined as

$$\mathrm{Re}_\tau = u_\tau (H/2)/\nu \tag{2}$$

in which $u_\tau = (\langle \tau_w \rangle / \rho)^{1/2}$ is the friction velocity. The quantity $\langle \tau_w \rangle$ is the wall-averaged wall shear stress which, in a void channel, would balance the large-scale pressure gradient along the main flow direction ξ, defined as $p_\xi = \Delta p / \Delta \xi$; i.e., one has $\langle \tau_w \rangle = (H/2) p_\xi$.

The Darcy friction coefficient (four times the Fanning friction factor) is defined as

$$f = \frac{4H}{\rho U^2} p_\xi \tag{3}$$

On the basis of the definitions given above for Re and Re_τ, one has also $f = 128(\mathrm{Re}_\tau / \mathrm{Re})^2$.

The local Nusselt number is defined as

$$Nu = h \frac{2H}{\lambda} \tag{4}$$

in which $h = q''_w/(T_b - T_w)$ is the local heat transfer coefficient, T_b being the fluid bulk temperature and T_w the local wall temperature. Wall-averaged values will be indicated as $\langle h \rangle$ and $\langle Nu \rangle$.

The Prandtl number was assumed to be 4, representative of water at ~40°C.

2 EXPERIMENTAL TECHNIQUE

2.1 Scaled-up spacers

As in our previous work on overlapped spacers [8], and for the reasons better discussed therein, experiments were conducted on a purpose built, scaled-up spacer-channel configuration, Figure 2(a). It was manufactured from commercial black rubber wire, 5 mm in diameter, commonly used for O-ring seals. The resulting distance between the plane channel walls was ~11 mm. The pitch of the wire net was ~22 mm, giving a pitch-to-height ratio P/H of ~2.

2.2 Test section

Experimental apparatus and TLC-based thermography have amply been discussed in previous papers [8, 28], so that only a concise summary will be given here.

Figure 3(a) shows the test section. Two channels, whose walls are 20 mm thick Plexiglas® slabs, are separated by a 1 mm thick polycarbonate layer. Hot fluid flows through the lower, spacer-filled, channel. A TLC sheet is interposed between the spacer and the polycarbonate layer, with its transparent side (~0.1 mm thick polyester layer) adhering to this latter. On the opposite side of the polycarbonate layer, cold fluid flows through the upper channel, which is void and ~3 mm thick.

2.3 Surface thermography by Thermochomic Liquid Crystals

The use of TLC to obtain surface temperature distributions is amply documented in the scientific literature [29, 30]. As an example, Figure 3(b) shows a typical image recorded for θ=45°, flow rate Q=60 l/h (Re≈215), bulk temperatures of the hot and cold channels equal to ~40°C and ~20°C, respectively, and flow from left to right. The image was recorded by a 18-Mpixel digital camera through the outer wall of the cold channel, the cold fluid, the polycarbonate layer, and the transparent polyester front cover of the TLC sheet. The two rectangles in colour, covering a total of 12 unit cells, correspond to the portion of the image that was digitally processed. RGB images were then converted into HSV (Hue, Saturation, Value) components, of which only the Hue component was assumed to be correlated with the wall temperature.

2.4 TLC calibration

The importance of *in situ* TLC calibration, and the different techniques that can be used to this purpose, are discussed in a recent paper by Abdullah *et al*. [31]. Here, calibration was performed by the isothermal method, as discussed in our previous paper [8]. A typical temperature vs. hue

dependence is shown in Figure 4. As indicated in the figure, a piecewise approximation with two 4th degree polynomials was used to fit the data. Note that a well defined hue-temperature relationship exists only in the Hue range 13 (red) through 168 (deep blue), and that this relationship is strongly nonlinear.

For the TLC sample used here (Hallcrest® R30C5W), the nominal colour play (from red start to blue start) was 30-35°C. As shown in Figure 4, the actual resolved temperature range was ~31-46°C. TLC sheets with different temperature ranges are commercially available.

The uncertainty relevant to the temperature of the TLC sheet mainly comes from the calibration procedure. The conversion of the Hue value into temperature requires two steps representing the main sources of uncertainty: (i) the water temperature measurement via Pt100 and (ii) the fitting of the Hue versus Temperature points plot with a suitable function. As declared by the manufacturer, Pt100 adopted uncertainty is 0.05 °C, while an uncertainty of 0.1 °C was estimated for the fitting. Therefore, the global uncertainty relevant to the temperature of the TLC sheet can be conservatively estimated as 0.15 °C. Other uncertainties as (i) the error arising by the Hue measurement via the photo-camera and (ii) the discretization error (1/256) associated with the 1-byte representation of Hue are small and can be reasonably neglected. Other details can be found in reference [28]

2.5. Derivation of the local heat transfer coefficient from wall temperature measurements

Figure 5 reports a schematic representation of the temperature profile across the different layers.An elementary analysis of the heat transfer process occurring through the various layers in series, under the assumption of one-dimensional transport (demonstrated to be reliable in [28]), gives first the local wall heat flux q" and then the local hot-side heat transfer coefficient h_h and Nusselt number as functions of the locally measured temperature T_w of the TLC sheet once the bulk temperatures T_h, T_c and the cold-side heat transfer coefficient are known:

$$q'' = \frac{T_w - T_c}{r} \tag{5}$$

$$h_h = \frac{q''}{T_h - T_w} \tag{6}$$

$$Nu_h = h_h \frac{d_{eq}}{\lambda} \tag{7}$$

in which r is an overall external thermal resistance consisting of the conductive thermal resistances s/λ of the thermochromic liquid crystal film (*TLC*) and of the polycarbonate layer (*pol*), in series with the convective thermal resistance $1/h_c$ associated with the cold channel:

$$r = \frac{s_{TLC}}{\lambda_{TLC}} + \frac{s_{pol}}{\lambda_{pol}} + \frac{1}{h_c} \tag{8}$$

Here, T_h and T_c were measured by Pt100 RTDs at the inlet and outlet of the hot and cold channels and a linear variation of T_h and T_c along the flow direction was assumed, as justified by the fact that estimated relaxation lengths are far larger than the test section length, especially at large flow rates. As a matter of fact, the uncertainty relevant to this estimation increases as the flow rate decreases. The convection coefficient h_c was estimated by the Dittus-Bölter correlation ($Nu=0.023\ Re^{0.8}\ Pr^{0.4}$) written for turbulent flow in the cold channel; a sensitivity analysis showed that the value of h_h calculated by Eq. (6) is only a weak function of the value used for h_c. The value of $6.24 \cdot 10^{-3}$ m^2K/W was thus computed for the overall external thermal resistance r. Further details on the experimental since $1/h_c$ is only a minor contribution to r. An uncertainty analysis of the above method can be found in reference [28].

2.6 Distributions obtained by digital image processing

As an example of the information that can be extracted from the pictures by digital image processing, Figure 6 reports unit cell distributions obtained for $P/H=2$, $\theta=90°$ and flow rate ~60 l/h (yielding a bulk Reynolds number Re≈215). The flow is from left to right. Graph (a) is a picture of the active, TLC-covered wall, in which saturation was enhanced for clarity purposes. Graph (b) shows the distribution of hue H extracted from (a). Graph (c) shows the wall temperature T_w derived

from H using the calibration curve in Figure 4. Finally, graphs (d), (e) and (f) report the distributions of wall heat flux q''_w, heat transfer coefficient h_h and Nusselt number Nu_h, respectively, derived from T_w using Eqs. (5-8).

2.7 Pressure drop measurements

Pressure drops in the hot fluid side were measured by using two longitudinally spaced tappings, located along the test section mid-line and 50 cm apart, and a Fuji Electric FCX-AII® differential manometer with a response of ~7.4 μA/Pa. Pressure drops were generally very small (e.g. 25 Pa at Re=350) and thus could be measured only with a limited accuracy, especially at the lower flow rates.

3 COMPUTATIONAL METHOD

In the present study, the computational domain was the unit cell shown in Figure 2(b). Mathematically, the problem was described by the continuity, Navier-Stokes and energy equations for a constant-property fluid. The "unit cell" treatment, discussed in previous papers [8], allowed periodicity conditions to be adopted for all variables at the opposite faces of the computational domain. All simulations were conducted by the finite volume ANSYS-CFX14® code [32].

No slip conditions (u_i=0) were imposed at the top and bottom walls and on the filaments' surface. As regards the thermal boundary conditions, the bottom wall and the filaments were assumed to be adiabatic (q''=0), while at the top wall a Cauchy (mixed) condition was imposed:

$$T_w - T_c = r\, q''_w \tag{5}$$

mimicking the experimental boundary condition, and choosing for the outer temperature T_c (19°C) and the thermal resistance r ($6.24 \cdot 10^{-3}$ m^2K/W) values representative of those holding in the experiments. Also the spacer sizes were the same as the experimental ones and the fluid was assumed to be water at 39°C with physical properties ρ=992.5 kg/m^3, c_p=4186 J/(kgK), λ=0.5985

W/(mK), μ=6.625×10^{-4} Pa·m, yielding a Prandtl number of 4.63. Finally, as in the parallel experiments, two orientations of the main flow with respect to the spacer filaments of the upper layer were considered (0° and 45°).

In preliminary studies, fluid flow was found to be steady up to friction velocity Reynolds numbers Re_τ of ~80, corresponding to bulk Reynolds numbers of ~240-270 depending on the flow attack angle. The same studies showed that, in this range, grid-independent results were obtained by using ~10^6 finite volumes. Therefore, in this range simulations were conducted in steady-state mode, while the number of finite volumes was conservatively increased to ~1.7×10^6. Unlike the corresponding overlapped-spacer geometry [8], the present one could not be discretized with purely hexahedral volumes; a hybrid grid was thus used, in which tetrahedral volumes were used in the regions surrounding the filaments (~30% of the overall volume of the computational domain) and hexahedral volumes in the remaining regions. Figure 2(c) reports a detail of the computational grid.

For larger values of Re_τ a time-dependent behaviour was observed, indicating the loss of stability of the base steady-state flow. Periodic flow was obtained for $\mathrm{Re}_\tau \approx$ 100-120 in the case θ=0° (bulk Reynolds number ~315-390) and for $\mathrm{Re}_\tau \approx$ 90-110 in the case θ=45° (bulk Reynolds number ~320-420). Simulations were also extended to incipient chaotic (turbulent) flow, obtained, in particular, for Re_τ = 140 in the case θ=0° (bulk Reynolds number 478) and for Re_τ = 120 in the case θ=45° (bulk Reynolds number 465). As the following “Comparison” Section shows, predictions for unsteady flow in the range investigated do not exhibit any change of trend with respect to lower-Re, steady-state, results and show a comparable degree of agreement with experimental data.

4 COMPARATIVE RESULTS

4.1 Nusselt number distributions

Figure 7 reports experimental (EXP) and predicted (CFD) pseudo color maps of the hot-side Nusselt number distributions on the active wall (Nu_h) for θ=0° and increasing Reynolds number. The inset shows the corresponding woven filament arrangement and main flow direction. Graphs (a), (c) and (e) on the right show CFD results for Re_τ=20 (Re=32), Re_τ=80 (Re=240) and Re_τ=140 (Re=478), respectively (the discontinuities observed in the computational plots in this and in the following figures are due only to graphic interpolation issues at the boundaries between regions gridded by tetrahedra and hexahedra). It can be observed that, as Re increases, the predicted Nu_h distributions remain roughly self-similar while their levels increase significantly. Graph (e), relevant to Re_τ=140 (Re=478), corresponds to an instantaneous field extracted from a chaotic flow, which is reflected in the irregular shape of the contours.

Graphs (b) and (d) on the left are experimental results for Q=60 l/h (Re≈215) and Q=150 l/h (Re≈520), respectively. Note that experimental results were not obtained for low Reynolds numbers comparable to that in graph (a). Experimental Nu_h distributions and levels are close to their computational counterparts for comparable Reynolds numbers. The main differences regard the values of Nu_h maxima, which are somewhat overestimated by the numerical simulations, and the narrow regions of high Nu_h predicted by CFD along the diagonal parallel to the main flow, which are not present in the experimental data.

The subsequent Figure 8 reports experimental and predicted Nu_h distributions for θ=45° and increasing Reynolds number. As above, the inset shows the woven filament arrangement and the main flow direction. Graphs (a), (c) and (e) on the right report CFD results for Re_τ=20 (Re=36), Re_τ=80 (Re=273) and Re_τ=120 (Re=465), respectively. As in the case θ=0°, it can be observed that, as Re increases, the predicted Nu_h distributions remain roughly self-similar while their levels

increase. Graph (e), relative to Re_τ=120 (Re=465), corresponds to an instantaneous field extracted from a chaotic flow, as revealed by the irregular shape of the contours.

Graphs (b) and (d) on the left are experimental results for Q=80 l/h (Re≈280) and Q=150 l/h (Re≈540), respectively. Also for this orientation, experimental results were not obtained at low Reynolds numbers comparable to that in graph (a). Experimental Nu_h distributions and levels are in general agreement with their computational counterparts for comparable Reynolds numbers. The main differences regard the values of Nu_h maxima, which – as in the case θ=0° - are somewhat overestimated by the numerical simulations, and the regions of high Nu_h predicted by CFD on the top side of the cell slightly upstream of the contact region with a filament, which are not clearly visible in the experiments.

4.2 Mean Nusselt number

Figure 9 summarizes all experimental and computational results for the wall-averaged hot-side Nusselt number at the top (active) wall of the unit cell, $\langle Nu_h \rangle$. Computational results start from a very low bulk Reynolds number (Re≈2). Under these conditions (creeping flow), $\langle Nu_h \rangle$ is almost independent of Re, as in parallel flow, but exhibits values depending on the flow attack angle and much higher than the exact (analytical) $\langle Nu_h \rangle$ for parallel flow in a plane channel, which is ~5.15 for the present mixed boundary condition characterized by $r/(D/\lambda)$≈0.75 [33]. At Reynolds numbers for which experimental data are available for comparison, CFD results generally compare favourably with these latter, with only some overprediction (~20%) for the case at Re≈150 and θ=0° (which is the only experimental result obtained for such low flow rates), and show a similar trend with Re. One possible reason for this overestimation is that, as discussed in [28], the experimental derivation of the local heat transfer coefficient from the local temperature implies some sources of uncertainty, among which at least one (the estimate of the local bulk temperatures from the measured inlet and outlet temperatures) is likely to increase with decreasing flow rate, as

the longitudinal bulk temperature profiles deviate from linearity. Moreover, CFD and experimental results exhibits a larger disagreement for θ=0-90° than for θ=45°, although this effect is really small (~10% in the average Nu). Simulations currently in progress suggest that this behaviour may depend on the large sensitivity of the heat transfer coefficients to the flow attack angle in the proximity of θ=0° (or 90°), so that small constructive imperfections of the experimental scaled-up spacer may cause large differences in the results.

As shown in Figure 9, for Re>500 only experimental data exist and they exhibit a power-law $Re^{0.5}$ behaviour, with the exception of the two or three highest-Re values (which, however, may be affected by accuracy issues since they correspond to the highest flow rates that could be investigated). Note that a mean Nusselt number increasing roughly as $Re^{0.5}$ has been reported for different spacers by the present [8, 28] and other authors [34, 35].

4.3 Friction coefficient

Figure 10(a) reports all experimental and computational results concerning the Darcy friction coefficient *f* as a function of the bulk Reynolds number. Up to Re≈10 (i.e., under conditions of creeping flow), computational results follow almost exactly a Re^{-1} trend and show no difference between the two orientations. For larger Re, they increasingly deviate from this trend and merge smoothly, especially for θ=0°, with the experimental results (some underprediction can be observed for θ=45°). For Re larger than ~200-300, when unsteady flow is expected, results tend to follow a power law trend with an exponent of ~ -0.37.

In Figure 10(b), the friction coefficient is normalized by the value that it would attain in a plane channel void of spacers under parallel flow conditions (96/Re). The figure shows that the pressure loss enhancement produced by the spacer (for a given flow rate) is ~14.6 for very low Re (creeping flow), as reported for the same geometry but in the context of Reverse Electrodialysis by Gurreri *et al*. [36], and increases with Re following roughly a power law of exponent 0.6, attaining values

above 100 at the highest flow rates investigated. Note that, in either graph, the transition from steady to unsteady and turbulent flow occurring at Re≈300 (as predicted by CFD and confirmed by visual observations of the temperature patterns in the experiments), is not associated to any obvious change in value or slope of the friction coefficient. This confirms that, in complex geometries, transition occurs smoothly (in bifurcation theory language, supercritically) and may well be associated to no relevant discontinuity in global quantities.

4.4 Flow and temperature fields

Flow attack angle θ=0°

The following Figures 11 through 13 report selected examples of the flow and temperature fields predicted by CFD for woven spacers with P/H=2, θ=0° and increasing flow rates.

In particular, Figure 11 is for Re_τ=5, yielding creeping flow at a bulk Reynolds number Re of ~2.3. Graph (a) shows a vector plot of the in-plane velocity and contours of the normal velocity for a plane parallel to the main flow direction. In this and the following figures, the insets show the location and orientation of the selected planes and the velocity normal to each plane is made dimensionless by the mean velocity U. Due to the negligible inertial effects, the flow reattaches almost immediately downstream of the transverse filament, no separation region exists and the secondary flow pattern is almost symmetric between the upstream and downstream directions. Graph (b) reports the temperature distribution on the same plane and shows an almost parallel stratification with little non-uniformity of the thermal boundary layer thickness near the upper, thermally active, wall. Graphs (c) and (d) are corresponding plots for a plane orthogonal to the main flow direction. The velocity plot (c) shows that, at this low Reynolds number, the longitudinal spacer filaments act almost as impervious vertical walls, dividing the flow passage area into separate, roughly rectangular, ducts. The temperature distribution (d) shows that large spanwise temperature gradients exist and that the thermal boundary layer thickens immediately above the

longitudinal filaments. Graph (e) reports flow streamlines; lines entering the unit cell from different side boundaries are marked with different colours. The figure shows that, despite the low Reynolds number, a large fraction of the streamlines entering the unit cell from above a transverse filament, i.e. close to the upper, cold wall, exit the cell from below the next filament and *vice versa*, thus causing considerable cross-stream mixing and enhancing heat transfer with respect not only to a void, parallel-walled, channel but also to a channel filled with an overlapped spacer of the same pitch [36].

Figure 12 reports corresponding results for Re_τ=80, yielding a bulk Reynolds number Re of ~240. The flow is still steady, but inertial effects are now obvious. Graph (a), reporting vectors of the in-plane velocity and contours of the normal velocity for a plane parallel to the main flow direction, shows large stagnant flow regions in the wake of the transverse filaments; in the same wake regions, the corresponding temperature distribution in graph (b) shows inverse thermal stratification, with masses of hot fluid interposed between the upper wall and the relatively cold midplane. The thermal boundary layer adjacent to the upper wall is now much thinner than in the previous, low Reynolds number, case. In the plane orthogonal to the main flow direction, the streamwise velocity, graph (c), exhibits now two distinct maxima on the two sides of each longitudinal filament. These maxima are shifted downwards in the left half of the cross section, in relation to the fact that in this half the fluid enters the cell from below the upstream transverse filament, and upwards in the right half, where the fluid enters the cell from above the same transverse filament. In the same plane, large secondary velocities are visible, following the inclination of the nearest longitudinal filament and thus moving upwards in the left half of the section and downwards in the right half. The temperature distribution, graph (d), exhibits a large spanwise variation of the thermal boundary layer thickness along the cold wall, and confirms that large blobs of hot fluid are convected towards the upper wall (and *vice versa*) by the secondary motion in graph (c). Bulk-to-wall temperature differences are now much lower than in the case Re_τ=5 in Figure 11, i.e. temperature polarization is highly reduced. The flow streamlines in graph

(e) are much less uniform in the spanwise direction than in the previous case and show regions of recirculation.

The instantaneous flow and temperature fields computed at larger Reynolds numbers, corresponding to time-dependent (periodic or turbulent) flow, are not too dissimilar from those relevant to Re_τ=80 (apart, of course, from irregularities related to the unsteadiness), and thus are not reported for brevity. As expected, they show an increasing thinning of the thermal boundary layer thickness, i.e. a decreasing temperature polarization.

Flow attack angle θ=45°

Figures 13 and 14 report selected examples of the flow and temperature fields predicted for woven spacers with P/H=2, θ=45° and different flow rates. As in the previous figures 11 and 12, insets show the location and orientation of the selected planes and the normal velocity is made dimensionless by the mean velocity U.

Figure 13 is for Re_τ=5, yielding creeping flow at about the same bulk Reynolds number Re (~2.3) as in the case θ=0°. Graph (a) shows a vector plot of the in-plane velocity and contours of the normal velocity for a plane parallel to the main flow direction. Note that, in this configuration, this plane forms an angle of 45° with the filaments. As in Figure 11(a), due to the negligible inertial effects, the flow reattaches almost immediately downstream of the transverse filament, no separation region exists and the secondary flow pattern is almost symmetric between the upstream and downstream directions. The temperature distribution on the same plane, graph (b), exhibits an almost parallel stratification with little non-uniformity of the thermal boundary layer thickness near the upper, thermally active, wall (apart from the wall regions immediately adjacent to the filaments). A global distortion of the isotherms exists near the bottom (adiabatic) wall, where it does not significantly affect heat transfer. Graphs (c) and (d) are for a plane orthogonal to the main flow direction. The velocity plot (c) shows a simple, Poiseuille-like, distribution of the streamwise

velocity, similar to that expected in a rectangular channel; however, a weak secondary circulation is also visible, consisting in a counter-clockwise rotation of the fluid (as viewed from downstream, see inset) around the left filaments and in an opposite, clockwise rotation around the right ones. The temperature distribution (d) shows a global distortion of the isotherms induced by the above secondary flow, which involves also the region adjacent to the upper, thermally active wall thus affecting heat transfer. Graph (e) shows that for this orientation, despite the low Reynolds number, significant mixing and streamline bifurcation occurs not only in the cross-stream (vertical) direction but also in the lateral direction, giving rise to a characteristic X-shape of the fluid trajectories.

Figure 14 reports corresponding results for Re_τ=80, yielding steady-state flow at a bulk Reynolds number Re of ~273. Graph (a), reporting vectors of the in-plane velocity and contours of the normal velocity for a plane parallel to the main flow direction, shows that, despite the large Reynolds number, wake effects downstream of the filaments are small thanks to the 45° orientation of the obstacles with respect to the main flow (compare with Figure 12(a) for θ=0°). The corresponding temperature distribution in graph (b) shows a thin and relatively uniform thermal boundary layer near the top, cold wall and an almost uniform temperature elsewhere. In the plane orthogonal to the main flow direction, the streamwise velocity, graph (c), exhibits now two sharp maxima in the lower left and upper right corners of the cross section. The secondary flow, rotating counter-clockwise rotation around the left filaments and clockwise around the right ones, is so intense that it induces an opposite, clockwise swirl in the central region of the duct (note that its chirality is that of a left-handed spiral when viewed from upstream). The temperature distribution in the plane normal to the main flow direction, graph (d), shows the entrainment of near-wall (cold) fluid towards the bottom wall, yielding a significant reduction of heat transfer rates in the corresponding region of the wall, see also Figure 8(c). Streamlines, graph (e), exhibit much the same “X” shaped pattern as for the lower Reynolds number case in Figure 13(e), but are more irregular and show some recirculation.

Instantaneous flow and temperature fields computed at an arbitrary time for this orientation (θ=45°) and higher values of Re_τ, corresponding to time-dependent (periodic or turbulent) flow, do not differ substantially from those reported for the case Re_τ=80 in Figure 14.

5. CONCLUSIONS

The spacer investigated in this study consisted of two interwoven layers of mutually orthogonal cylindrical filaments with a pitch-to-channel height ratio of 2. Thus, this study complements a previous investigation [8] dedicated to *overlapped* spacers with the same pitch-to-height ratio and similar flow rates.

Experiments by thermochromic liquid crystals provided the distribution and the surface-averaged value of the heat transfer coefficient *h* on the thermally active wall for two orientations of the filaments with respect to the main flow (0° and 45°) and bulk Reynolds numbers Re in the range 200~2000. Parallel numerical simulations were conducted in the range Re≈2-500; steady-state flow was predicted for both orientations up to Re=240 (θ=0°) or 270 (θ=45°), while for larger values of Re the flow became first periodic and eventually chaotic.

Together, experiments and CFD simulations covered a very large interval of bulk Reynolds numbers ranging from ~2 to ~2000. In the range of overlapping, a very good agreement (better than that reported for non-woven spacers in previous work [8]) was obtained between experimental and computational results: the comparison concerned both local and global quantities. The 2D maps of the Nusselt number experimentally assessed via the TLC based technique were very well predicted by the CFD simulations both in terms of distribution and absolute values. Global data concerned the Darcy friction coefficient *f* and the average Nusselt number $\langle Nu_h \rangle$ as functions of the Reynolds number: both trends were in a good agreement, some discrepancies were observed only (i) at intermediate Re for the prediction of *f* at θ=45° and (ii) at low Re for the prediction of $\langle Nu_h \rangle$ at θ=0°.

As far as the comparison between the two different configurations is concerned, at very low Re the θ=45° configuration is much more efficient than that relevant to θ=0°: in particular, $\langle Nu_h \rangle$ for θ=45° is about twice that for θ=0°, while f is very similar. As Re increases, the gap in $\langle Nu_h \rangle$ for the two configurations gradually decreases (up to almost disappearing for Re>300); this effect reduces the θ=45° orientation convenience as Re increases. These findings are confirmed in the literature by CFD data (Re range 1-64) concerning the mass (i.e. electrolyte) transfer in thin spacer-filled channels for Reverse Electrodialysis applications [36], although in that case flux was imposed on both cross-stream boundaries (i.e. *bilateral mass transfer*). At the largest Re investigated (only by experiments), where the flow regime is expected to be fully turbulent, the two configurations exhibit very similar $\langle Nu_h \rangle$-Re and f-Re trends.

Acknowledgments

This work was partly funded (i) by the MEDIRAS project within the EU-FP7 research programme (contract number TREN/FP7EN/218938) and (ii) by the RED-Heat-to-Power project (Conversion of Low Grade Heat to Power through closed loop Reverse Electro-Dialysis) within the EU Horizon 2020 programme (Project Number 640667: www.red-heat-to-power.eu). The authors are grateful to SOFIP SpA for their financial support and to Dr. Luigi Gurreri for his precious help with grid generation.

NOMENCLATURE

Symbol	Quantity
D_h	"Void" hydraulic diameter, $2H$
d	Spacer filament diameter ($=H/2$)
f	Darcy friction coefficient
h	Heat transfer coefficient, $q"_w/(T_b-T_w)$
H	Channel height
l	Spacer filament pitch
Nu	Nusselt number, hD_h/λ
Pr	Prandtl number
Q	Volume flow rate
$q"_w$	Wall heat flux
r	Overall external thermal resistance
Re	Bulk Reynolds number, UD_h/ν
Re_τ	Friction velocity Reynolds number, $u_\tau(H/2)/\nu$
s	Thickness
T	Temperature
U	Mean velocity in the void channel, $Q/(HW)$
u, v, w or u_j	Velocity components along x, y, z
u_τ	Friction velocity
W	Channel spanwise extent
x, y, z	Cartesian coordinates

Greek symbols

θ	Angle formed by the spacer with the main flow
λ	Thermal conductivity
μ	Viscosity
ν	Kinematic viscosity, μ/ρ
ξ	Distance along the flow direction
ρ	Density
τ_w	Wall shear stress

Subscripts

b	Bulk
c	Cold
h	Hot
poly	Polycarbonate sheet
TLC	Thermochromic Liquid Crystals
w	Wall (=hot side of TLC layer)
ξ	Main flow direction

Averages

$\bar{\Phi}$	Time average of the generic quantity Φ
$\langle\Phi\rangle$	Space average (e.g. on a plane) of Φ

REFERENCES

[1] A. Cipollina, M.G. Di Sparti, A. Tamburini, G. Micale., Development of a Membrane Distillation module for solar energy seawater desalination, *Chem. Eng. Res. Des.*, 90 (2012) 2101-2121.

[2] P. Xie, L.C. Murdoch, D.A. Ladner, Hydrodynamics of sinusoidal spacers for improved reverse osmosis performance, *J. Membr. Sci.*, 453 (2014) 92-99.

[3] M. Tedesco, A. Cipollina, A. Tamburini, W. van Baak, G. Micale., Modelling the Reverse ElectroDialysis process with seawater and concentrated brines, *Desalination and Water Treatment*, 49 (2012) 404–424.

[4] J. Schwinge, P.R. Neal, D.E. Wiley, D.F. Fletcher, A.G. Fane, Spiral wound modules and spacers: Review and analysis, *Journal of Membrane Science* 242 (2004) 129–153.

[5] J. Liu, A. Iranshahi, Y. Lou, G. Lipscomb, Static mixing spacers for spiral wound modules, *J. Membr. Sci.*, 442 (2013) 140–148.

[6] F. Li, W. Meindersma, A.B. de Haan, T. Reith, Novel spacers for mass transfer enhancement in membrane separations, *Journal of Membrane Science* 253 (2005) 1–12.

[7] R.D. Gustafson, J.R. Murphy, A. Achilli, A stepwise model of direct contact membrane distillation for application to large-scale systems: Experimental results and model predictions, *Desalination* 378 (2016) 14–27.

[8] A. Tamburini, M. Renda, A. Cipollina, G. Micale, M. Ciofalo, Investigation of heat transfer in spacer-filled channels by experiments and direct numerical simulations, *International Journal of Heat and Mass Transfer*, 93 (2016) 1190–1205.

[9] L. Martínez-Díez, M.I. Vázquez-González, Temperature and concentration polarization in membrane distillation of aqueous salt solutions, *Journal of Membrane Science* 156 (1999) 265-273.

[10] M. Amokrane, D. Sadaoui, C.P. Koutsou, A.J. Karabelas, M. Dudeck, A study of flow field and concentration polarization evolution in membrane channels with two-dimensional spacers during water desalination, *J. Membr. Sci.*, 477 (2015) 139-150.

[11] G. Schock, A. Miquel, Mass transfer and pressure loss in spiral wound modules, *Desalination*, 64 (1987) 339-352.

[12] J. Phattaranawik, R. Jiraratananon, A.G. Fane, C. Halim, Mass flux encement using filled channels in Direct Contact Membrane Distillation, *J. Membr. Sci*., (2001) 193-201.

[13] F. Li, W. Meindersma, A.B. de Haan, T. Reith, Optimization of commercial net spacers in spiral wound membrane modules, *J. Membr. Sci*., 208 (2002) 289–302.

[14] Y. Yun, J. Wang, R. Ma, A.G. Fane, Effects of channel spacers on Direct Contact Membrane Distillation, *Desalination and Water Treatment*, 34 (2011) 63-69.

[15] A. Tamburini, A. Cipollina, S. Al-Sharif, M. Albeyrutty, L. Gurreri, G. Micale and M. Ciofalo, Assessment of temperature polarization in Membrane Distillation channels by Liquid Crystal Thermography, *Desalination and Water Treatment*, 55 (2015) 2747-2765.

[16] C.P. Koutsou, S.G. Yiantsios, A.J. Karabelas, Direct numerical simulation of flow in spacer-filled channels: effect of spacer geometrical characteristics, *J. Membr. Sci.*, 291 (2007) 53–69.

[17] L. Martínez-Díez, M.I. Vázquez-González, F.J. Florido-Díaz, Study of membrane distillation using channel spacers, *Journal of Membrane Science* 144 (1998) 45-56.

[18] M. Johannink, K. Masilamani, A. Mhamdi, S. Roller, W. Marquardt, Predictive pressure drop models for membrane channels with non-woven and woven spacers, *Desalination*, 376 (2015) 41–54.

[19] A. Saeed, R. Vuthaluru, H. B. Vuthaluru, Investigations into the effects of mass transport and flow dynamics of spacer filled membrane modules using CFD, *Chem. Eng. Res. Des.*, 93 (2015) 79-99.

[20] S.K. Karode, A. Kumar, Flow visualization through spacer filled channels by computational fluid dynamics I. Pressure drop and shear rate calculations for flat sheet geometry, *J. Membr. Sci*., 193 (2001) 69–84.

[21] L. Gurreri, A. Tamburini, A. Cipollina, G. Micale, M. Ciofalo, CFD simulation of mass transfer phenomena in spacer filled channels for Reverse Electrodialysis applications, *Chem. Eng. Trans.*, 32 (2013) 1879-1884.

[22] L. Gurreri, M. Ciofalo, A. Cipollina, A. Tamburini, W. Van Baak, G. Micale, CFD modelling of profiled-membrane channels for Reverse Electrodialysis, *Desalination and Water Treatment*, 55 (2015) 3404–3423.

[23] S. Al-Sharif, M. Albeirutty, A. Cipollina, G. Micale, Modelling flow and heat transfer in spacer-filled Membrane Distillation channels using open source CFD code, *Desalination*, 311 (2013) 103–112.

[24] A. Mahdavifar, A. Pollard, J.G. Pharoah, S.B. Beale, Wall proximity effects on flow over a simple membrane spacer, *Computers & Fluids*, 88 (2013) 180–188.

[25] M. Shakaib, S.M.F. Hasani, I. Ahmed, R.M. Yunus, A CFD study on the effect of spacer orientation on temperature polarization in Membrane Distillation modules, *Desalination*, 284 (2012) 332–340.

[26] A. Tamburini, A. Parlapiano, A. Cipollina, M. Ciofalo, G. Micale, Temperature distribution analysis in spacer filled channels for Membrane Distillation, Procs. 7th Int. Symp. *Turbulence, Heat and Mass Transfer*, Palermo, Italy, 24-27 September 2012, pp. 299-302, K. Hanjalic, Y. Nagano, D. Borello and D. Jakirlic, eds, Begell House Inc., New York, 2012.

[27] A. Tamburini, G. Micale, M. Ciofalo, A. Cipollina, Experimental analysis via Thermochromic Liquid Crystals of the temperature local distribution in Membrane Distillation modules, *Chem. Eng. Trans.* 32 (2013) 2041-2046. Doi: 10.3303/CET1332341.

[28] A. Tamburini, P. Pitò, A. Cipollina, G. Micale, M. Ciofalo, A Thermochromic Liquid Crystals image analysis technique to investigate temperature polarization in spacer-filled channels for membrane distillation, *J. Membr. Sci.*, 447 (2013) 260-273.

[29] M. Ciofalo, I. Di Piazza, J. A. Stasiek, Investigation of flow and heat transfer in corrugated-undulated plate heat exchangers, *Heat and Mass Transfer* 36 (2000) 449-462.

[30] V.U. Kakade, G.D. Lock, M. Wilson, J.M. Owen, J.E. Mayhew, Accurate heat transfer measurements using Thermochromic Liquid Crystals. Part 2: Application to a rotating disc, *Int. J. Heat Fluid Flow* 30 (2009) 950–959.

[31] N. Abdullah, A. R. Abu Talib, A. A. Jaafar, M. A. Mohd Salleh, W. T. Chong, The basics and issues of Thermochromic Liquid Crystal Calibrations, *Experimental Thermal and Fluid Science* 34 (2010) 1089–1121.

[32] Ansys Inc., Ansys-CFX Reference Guide, Release 14.5 (2012).

[33] Mariagiorgia Floriana La Cerva, *Ottimizzazione di Canali con Spaziatori per Processi a Membrana mediante Termofluidodinamica Computazionale*, Tesi di Laurea Magistrale in Ingegneria Energetica e Nucleare, Università di Palermo (2015).

[34] A. R. Da Costa, A. G. Fane, D. E. Wiley, Spacer characterization and pressure drop modelling in spacer filled channel for ultrafiltration, *J. Membr. Sci.* 87 (1994) 79-98.

[35] J. Phattaranawik, R. Jiraratananon, A. G. Fane, Heat transport and membrane distillation coefficients in direct contact membrane distillation, *J. Membr. Sci*. 212 (2003) 177–193.

[36] L. Gurreri, A. Tamburini, A. Cipollina, G. Micale, M. Ciofalo, Flow and mass transfer in spacer-filled channels for reverse electrodialysis: a CFD parametrical study, *J. Membr. Sci*. 497 (2016) 300–317.

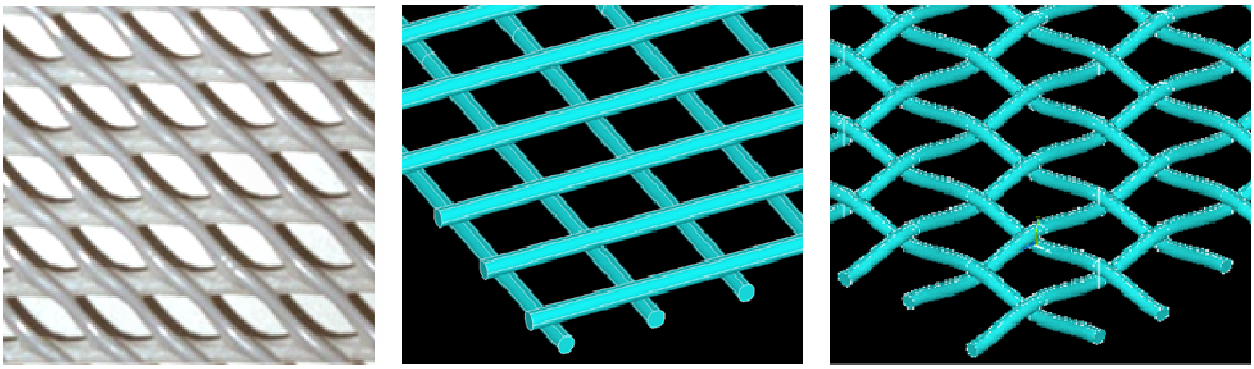

(a) (b) (c)

Figure 1 Different families of net spacers: a) extruded; b) overlapped; c) woven.

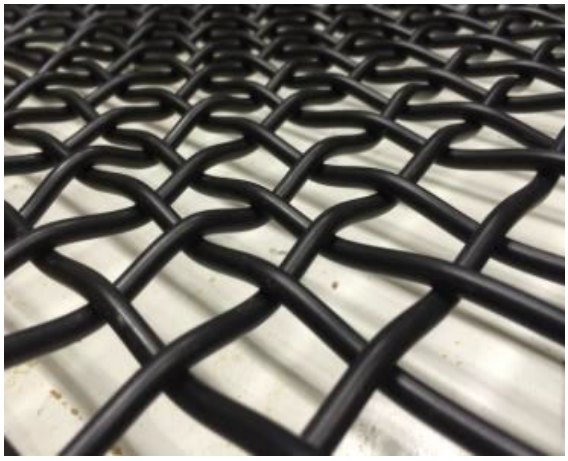

(a)

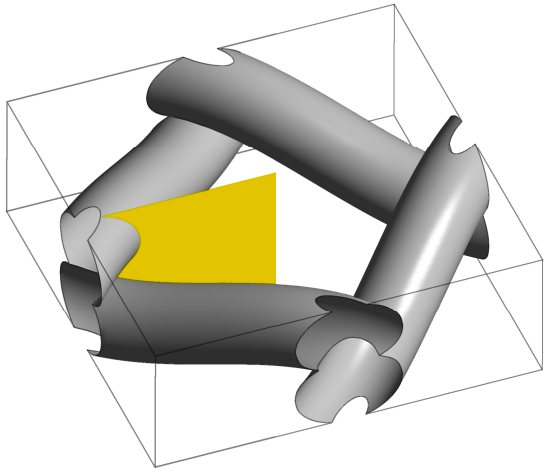

(b)

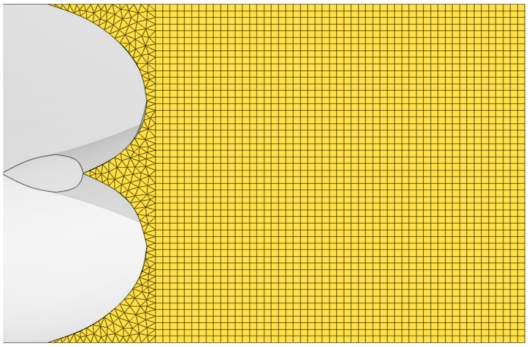

(c)

Figure 2 (a) Purpose built woven spacer (P/H=2); (b) unit cell used for the numerical simulations; (c) enhancement of the detail highlighted in (b), showing the hybrid computational grid.

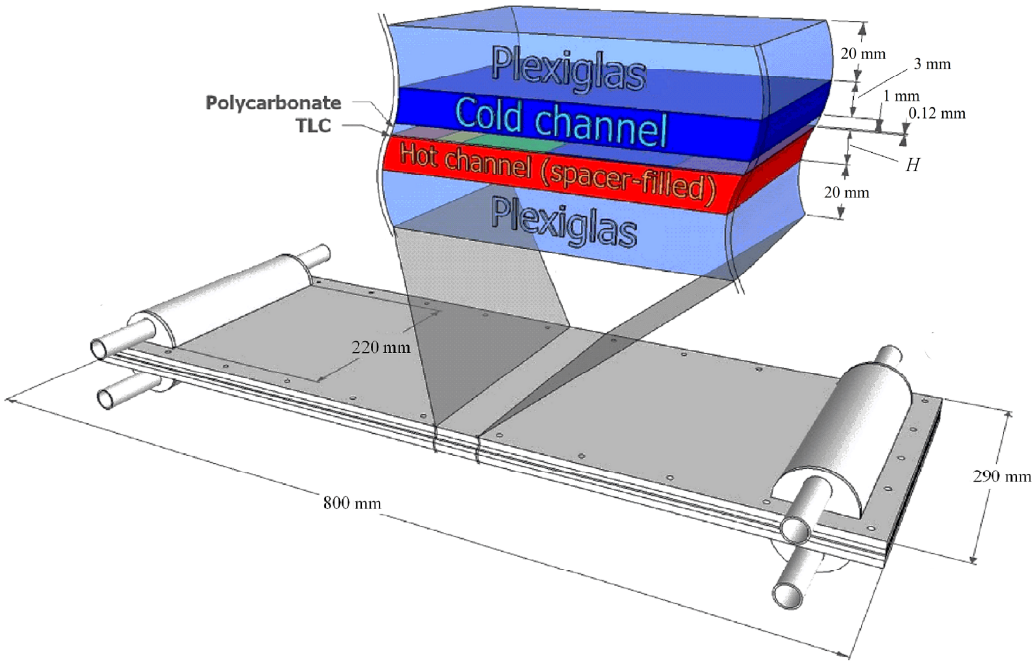

(a)

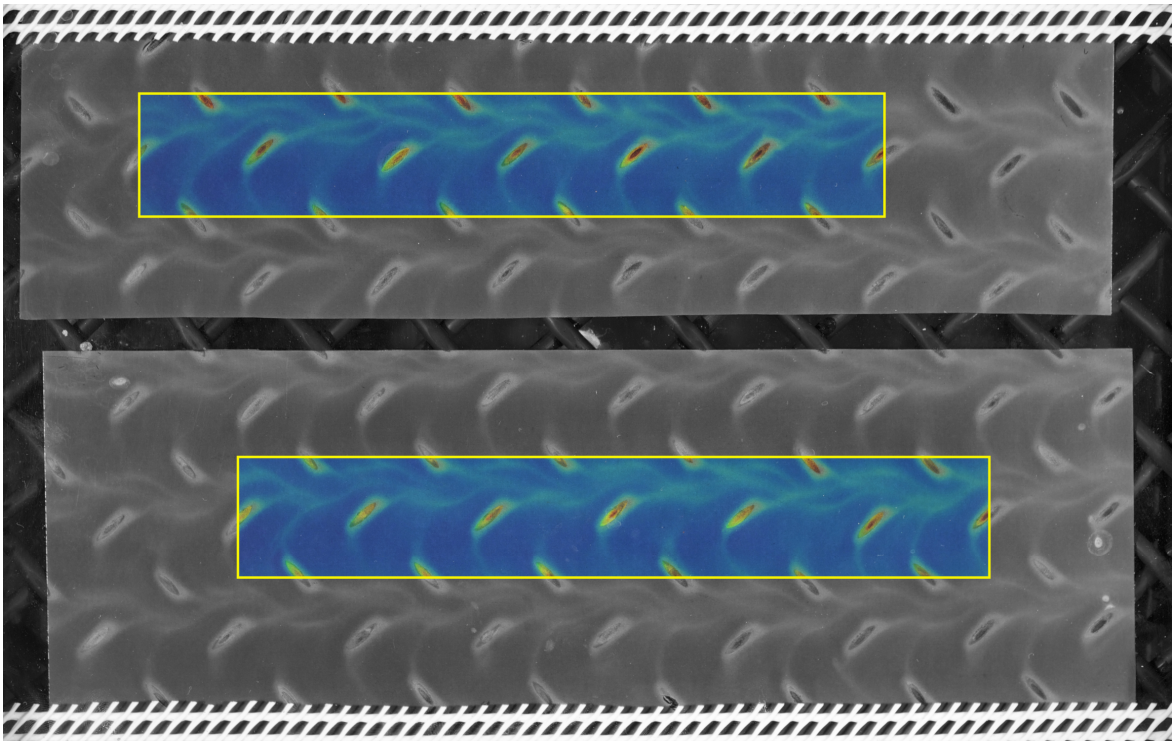

(b)

Figure 3 (a) Representation of the test section with an enhanced detail of the different layers; (b) typical image of the active wall partially covered with Thermochromic Liquid Crystals (θ=45°, flow rate Q=60 l/h yielding Re≈215, T_h≈40°C, T_c≈20°C, flow from left to right). The image regions used for temperature measurements are evidenced in colour.

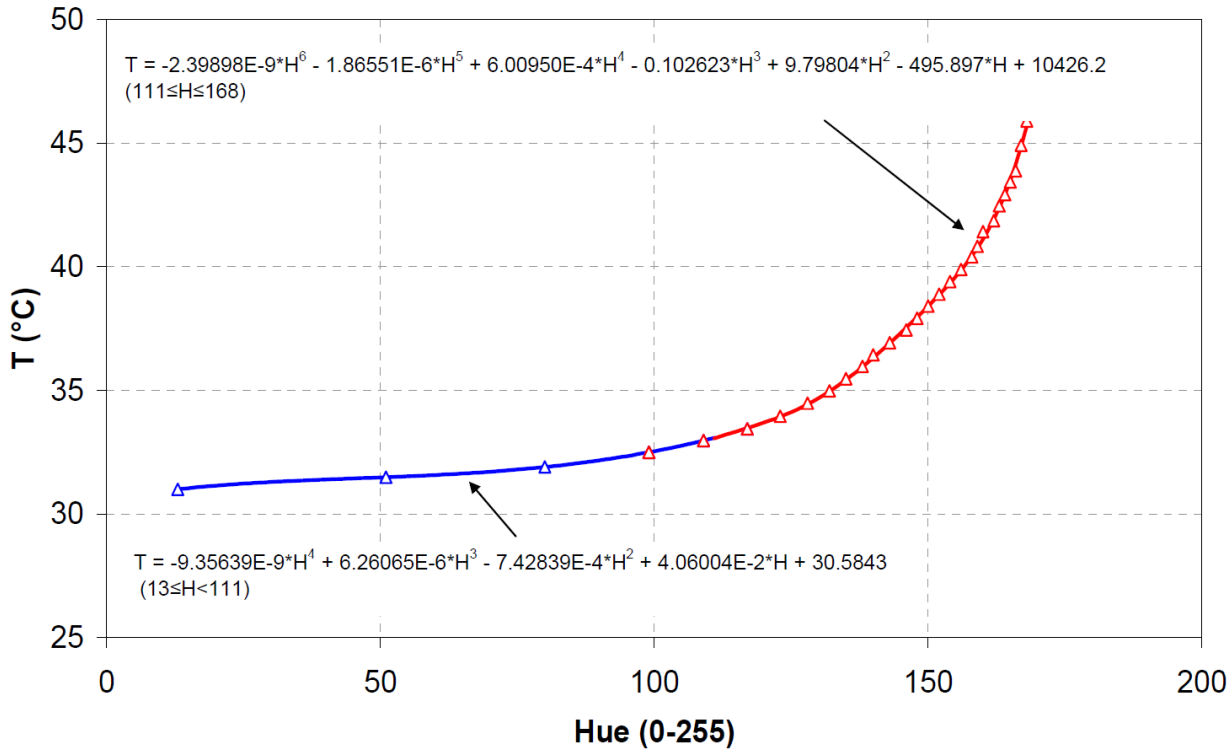

Figure 4 Typical *in situ* TLC calibration curve (tests conducted for θ=45°). A piecewise approximation using two 4th-order polynomials is also reported.

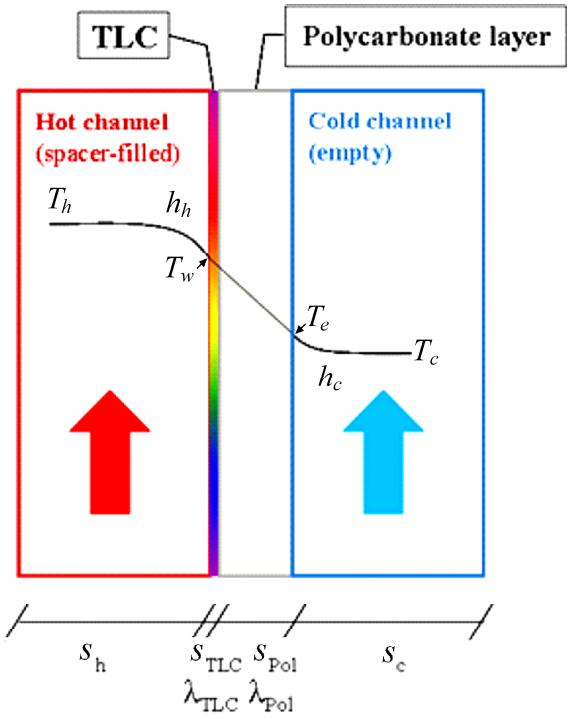

Figure 5 Sketch of the temperature profile across the different layers of the test section

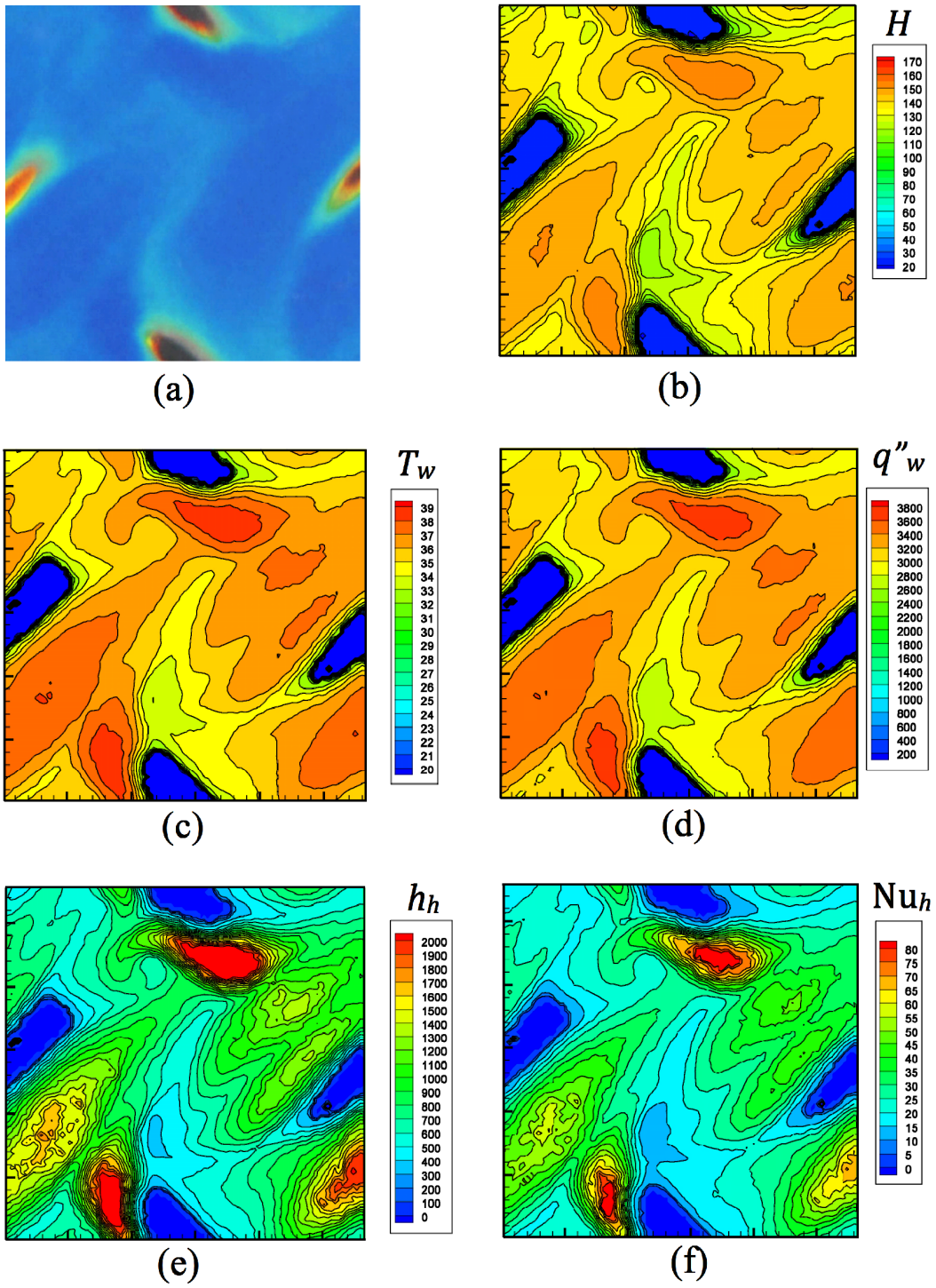

Figure 6 Distributions obtained by digital image processing for a unit cell of a woven spacer (P/H=2, θ=90°, Re≈215, flow from left to right). (a) picture of the TLC-covered wall. (b) Hue H extracted from (a). (c) Wall temperature T_w derived from H using the calibration curve in Figure 4. (d), (e), (f) Local distributions of wall heat flux q''_w, heat transfer coefficient h_h and Nusselt number Nu_h derived from T_w using Eqs. (5)-(7).

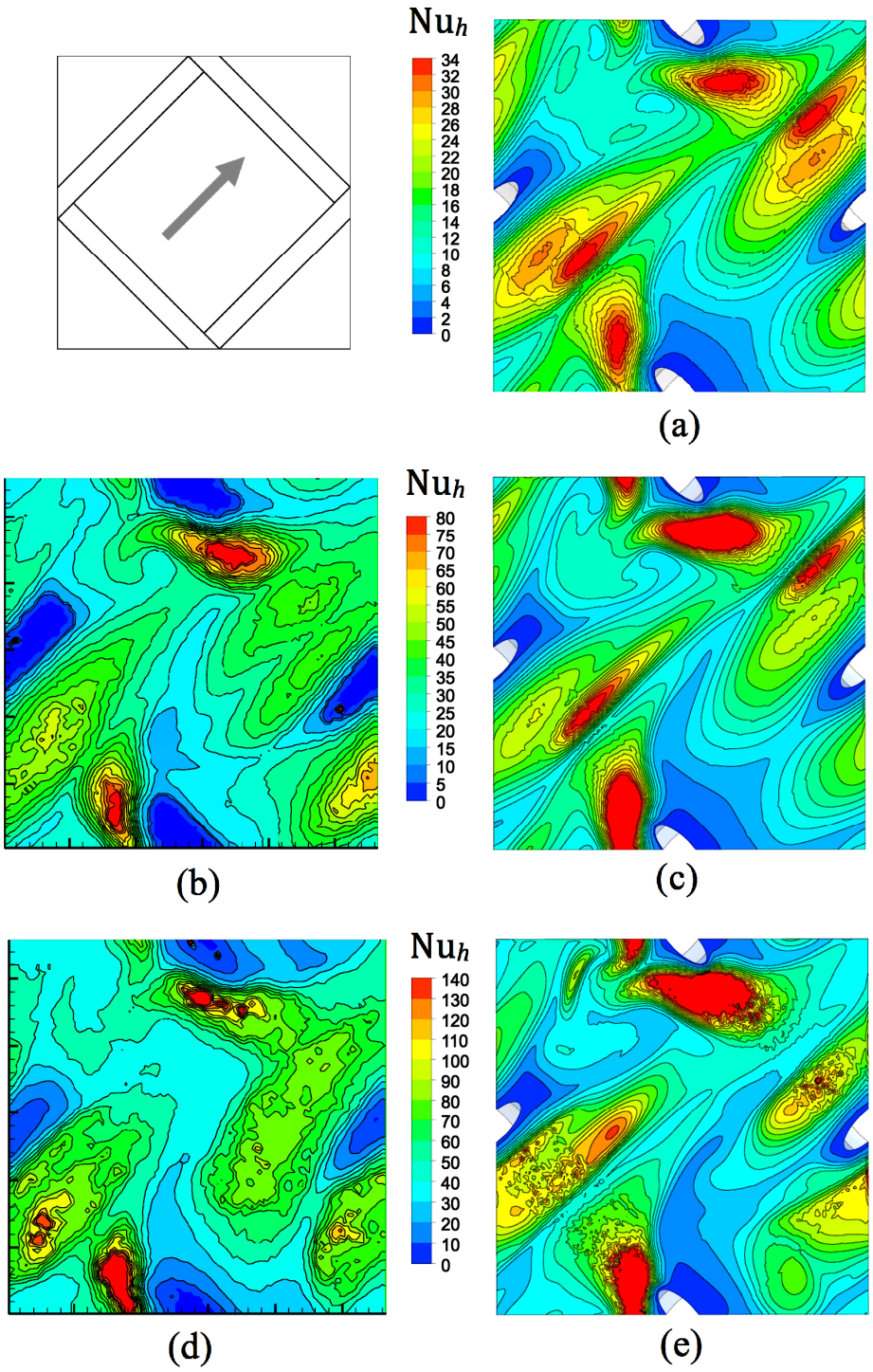

Figure 7 Experimental (EXP) and predicted (CFD) Nusselt number distributions on the active wall for θ=0° and increasing Reynolds number. (a) CFD, Re_τ=20 (Re=32); note that experimental results were not obtained for this low Reynolds number. (b) EXP, Q=60 l/h (Re≈215); (c) CFD, Re_τ=80 (Re=240). (d) EXP, Q=150 l/h (Re≈520); (c) CFD, Re_τ=140 (Re=478). The inset shows the woven filament arrangement and the main flow direction.

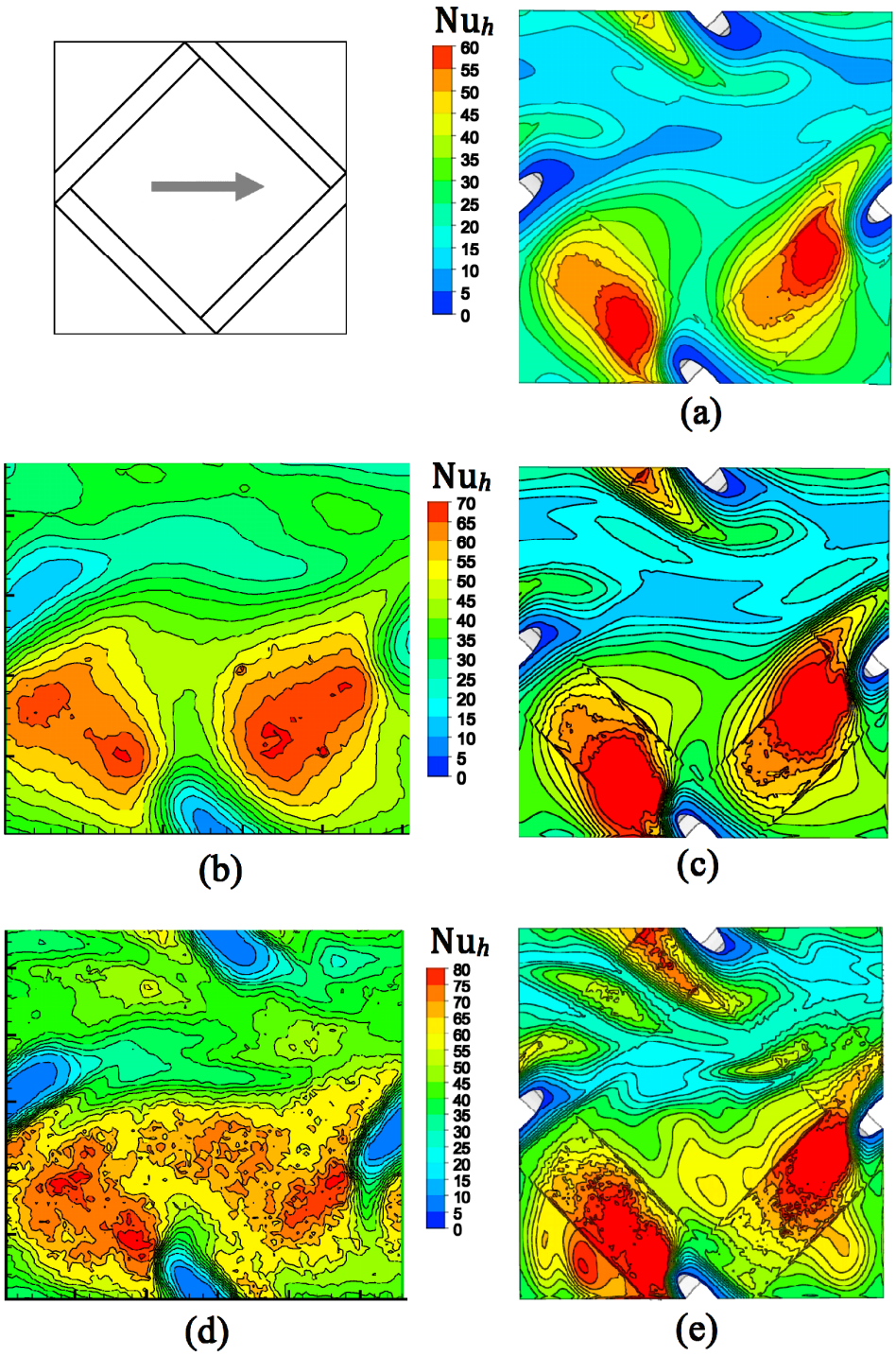

Figure 8 Experimental (EXP) and predicted (CFD) Nusselt number distributions on the active wall for θ=45° and increasing Reynolds number. (a) CFD, Re_τ=20 (Re=36); note that experimental results were not obtained for this low Reynolds number. (b) EXP, Q=80 l/h (Re≈280); (c) CFD, Re_τ=80 (Re=273). (d) EXP, Q=150 l/h (Re≈540); (c) CFD, Re_τ=120 (Re=465). The inset shows the woven filament arrangement and the main flow direction.

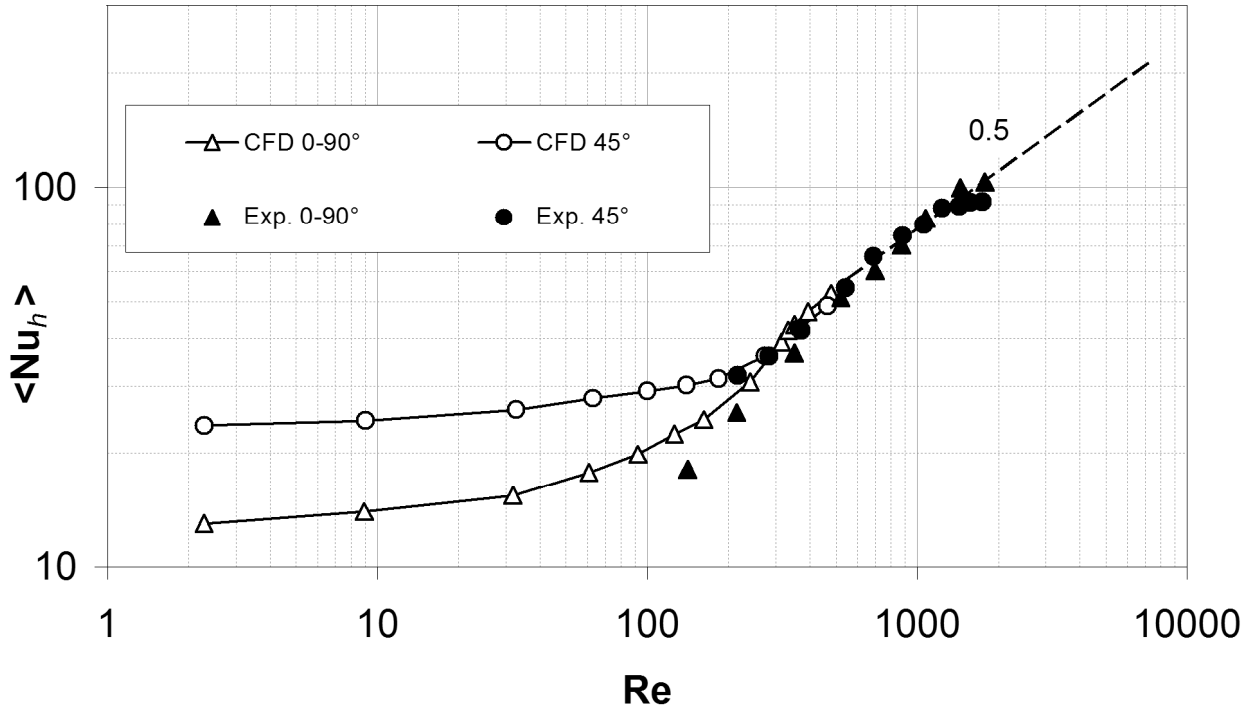

Figure 9 Mean Nusselt number for woven spacers with P/H=2, θ=0° or 45° and bulk Reynolds numbers in the range 2-2000. Solid symbols: experimental results. Hollow symbols: computational results. A power-law trend line is included.

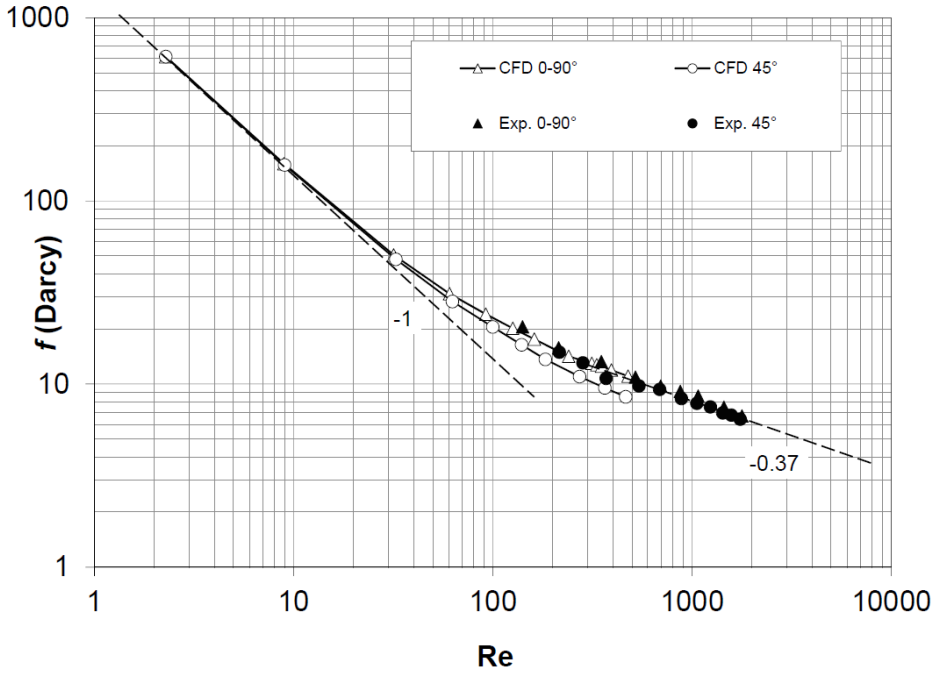

(a)

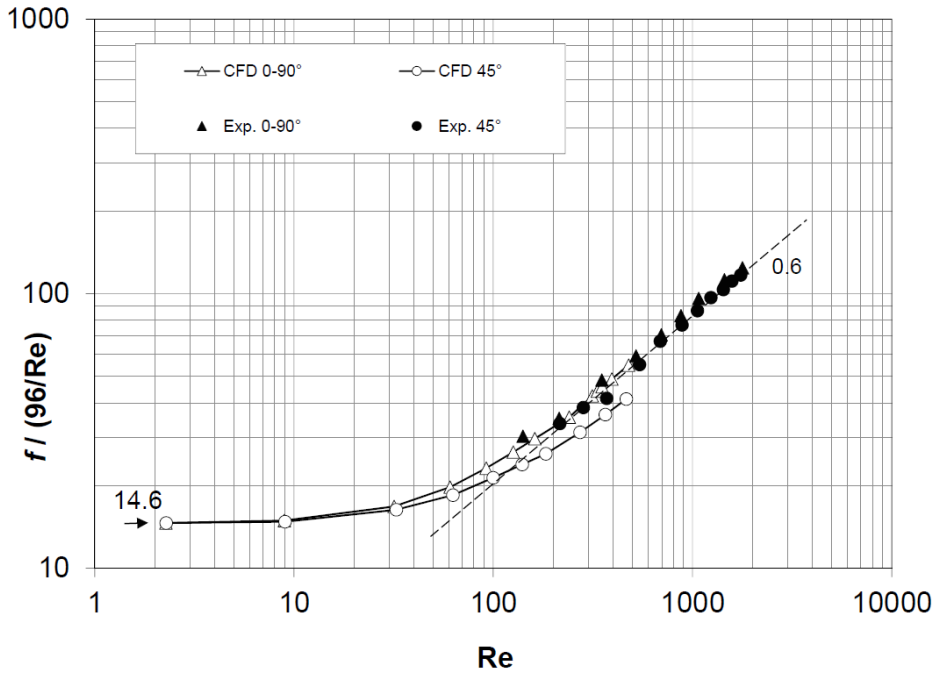

(b)

Figure 10 Darcy friction coefficient f for woven spacers with P/H=2 and θ=0° and 45°. Solid symbols: experimental results. Hollow symbols: computational results. (a) f as a function of Re in log-log scale (power-law trend lines are included). (b) f normalized by the void plane channel (parallel flow) coefficient 96/Re in log-log scale.

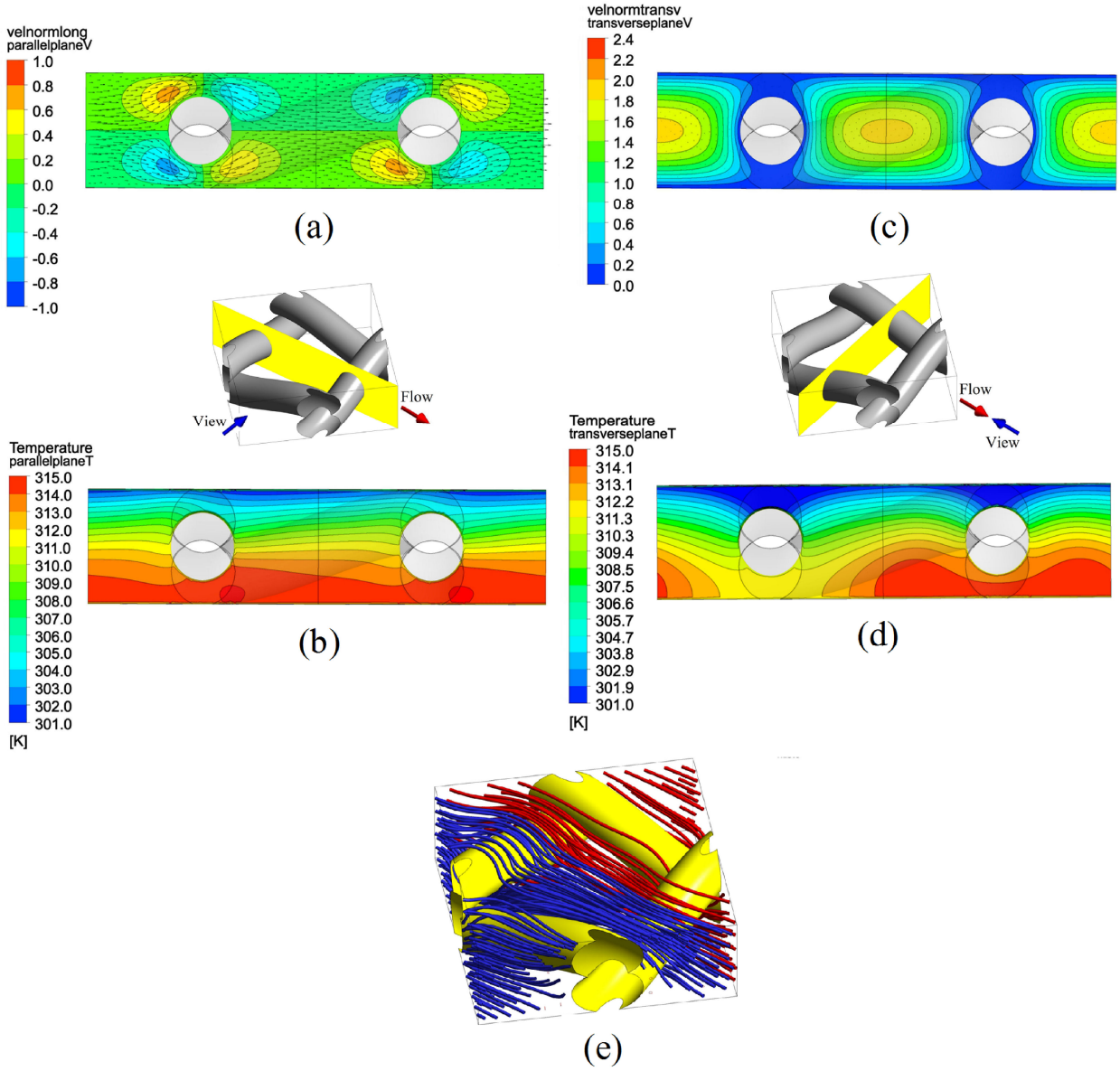

Figure 11 Flow and temperature field for woven spacers with P/H=2, θ=0°, Re_τ=5 (creeping flow at Re≈2.3). (a) Vector plot of the in-plane velocity and contours of the normal velocity for a plane parallel to the main flow direction (see inset on the left). (b) Temperature distribution on the same plane. (c) Vector plot of the in-plane velocity and contours of the normal velocity for a plane orthogonal to the main flow direction (see inset on the right). (d) Temperature distribution on the same plane. (e) Streamlines (lines entering the unit cell from different side boundaries are marked with different colours).

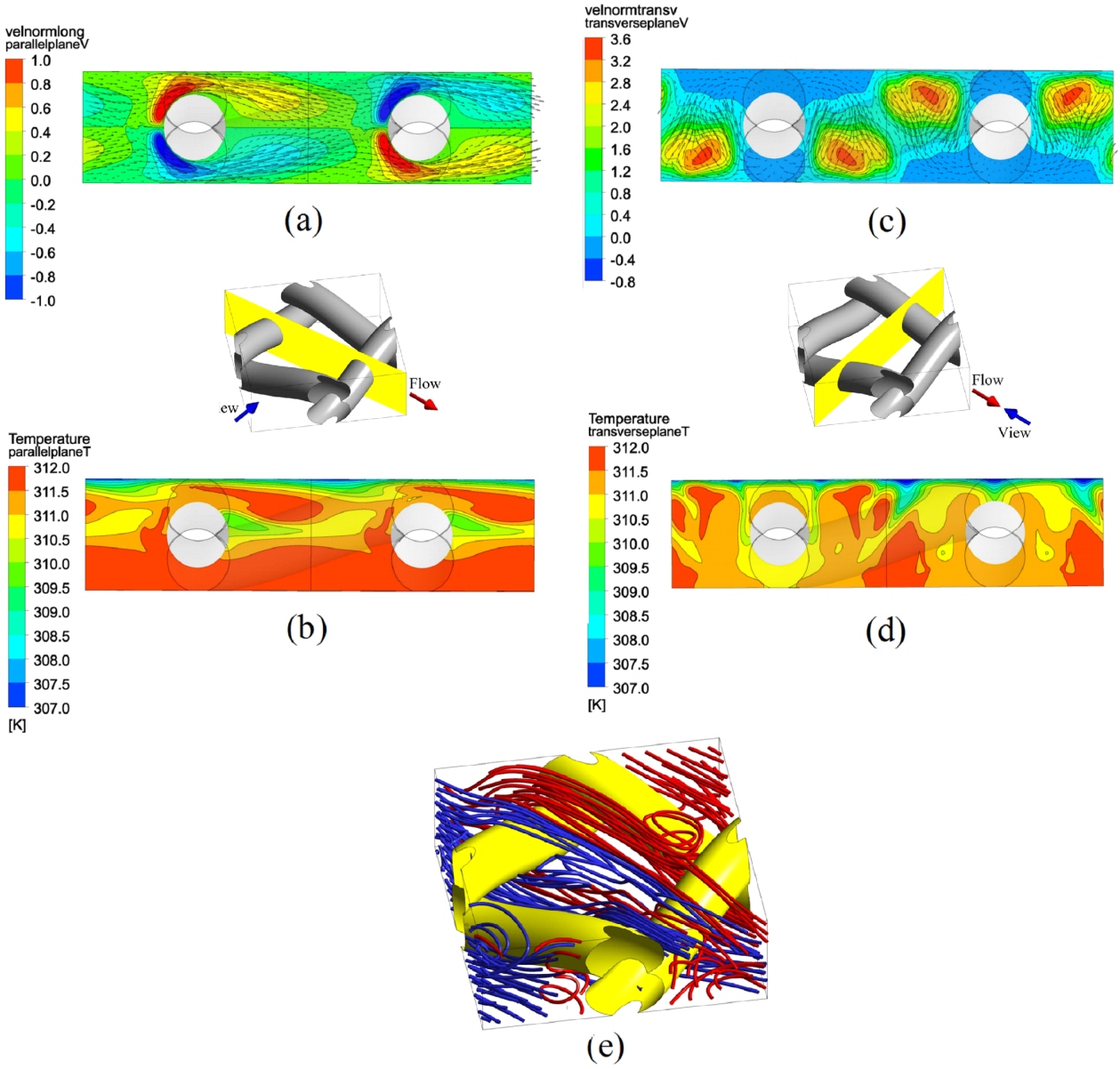

Figure 12 Flow and temperature field for woven spacers with P/H=2, θ=0°, Re_τ=80 (steady-state flow at Re≈240). (a) Vector plot of the in-plane velocity and contours of the normal velocity for a plane parallel to the main flow direction (see inset on the left). (b) Temperature distribution on the same plane. (c) Vector plot of the in-plane velocity and contours of the normal velocity for a plane orthogonal to the main flow direction (see inset on the right). (d) Temperature distribution on the same plane. (e) Streamlines (lines entering the unit cell from different side boundaries are marked with different colours).

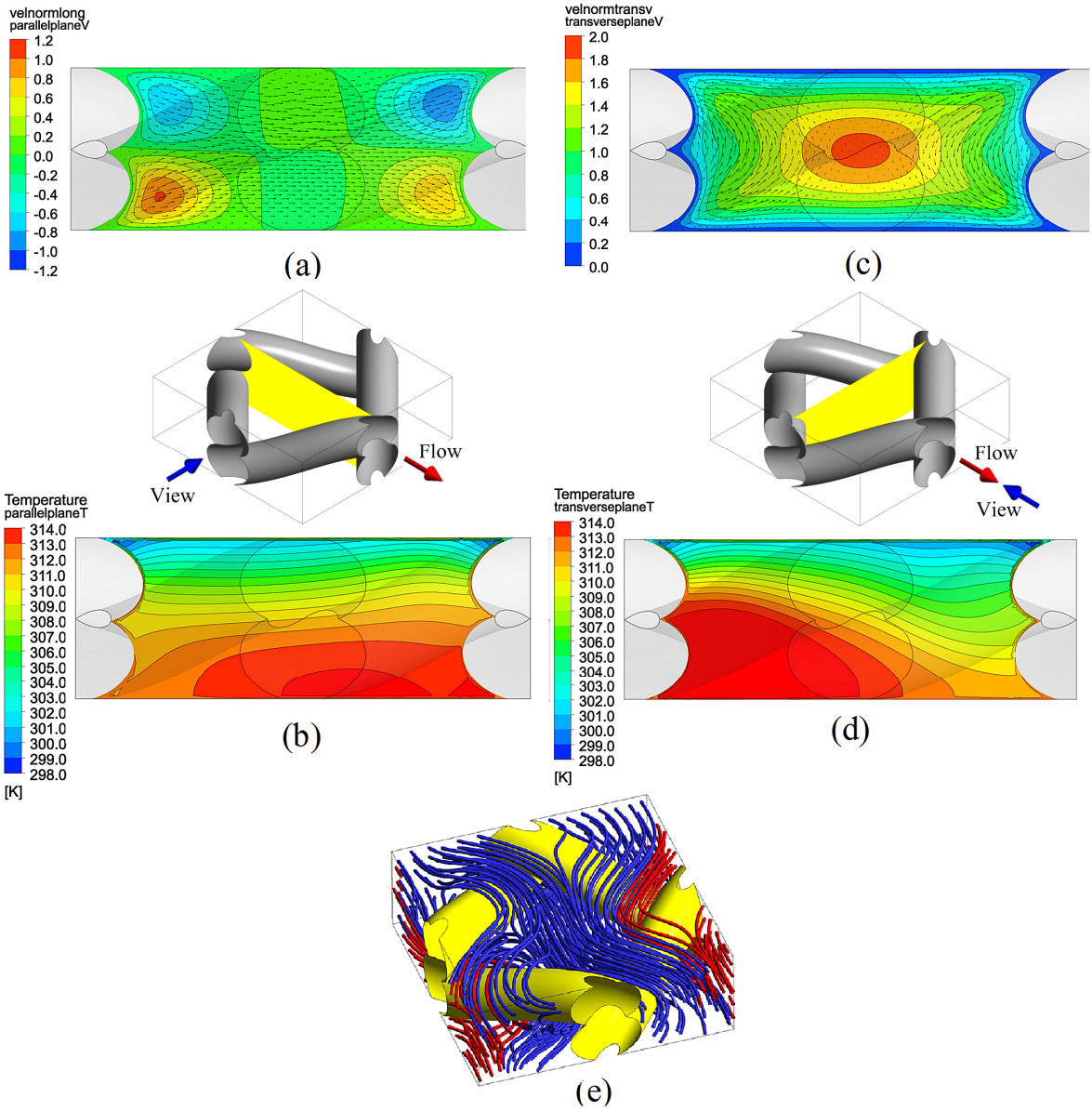

Figure 13 Flow and temperature field for woven spacers with P/H=2, θ=45°, Re_τ=5 (creeping flow at Re≈2.3). (a) Vector plot of the in-plane velocity and contours of the normal velocity for a plane parallel to the main flow direction (see inset on the left). (b) Temperature distribution on the same plane. (c) Vector plot of the in-plane velocity and contours of the normal velocity for a plane orthogonal to the main flow direction (see inset on the right). (d) Temperature distribution on the same plane. (e) Streamlines (lines entering the unit cell from different side boundaries are marked with different colours).

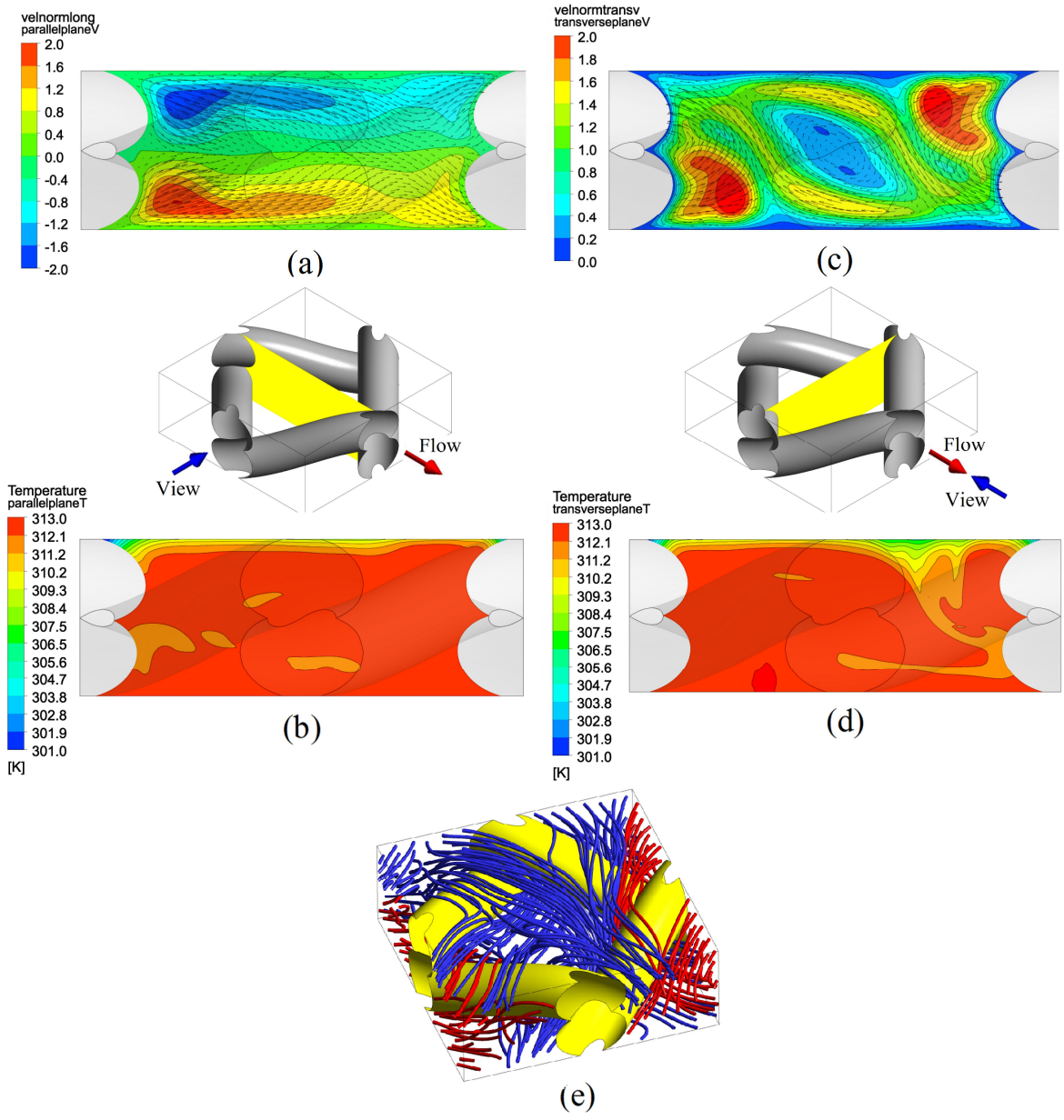

Figure 14 Flow and temperature field for woven spacers with P/H=2, θ=45°, Re_τ=80 (steady-state flow at Re≈273). (a) Vector plot of the in-plane velocity and contours of the normal velocity for a plane parallel to the main flow direction (see inset on the left). (b) Temperature distribution on the same plane. (c) Vector plot of the in-plane velocity and contours of the normal velocity for a plane orthogonal to the main flow direction (see inset on the right). (d) Temperature distribution on the same plane. (e) Streamlines (lines entering the unit cell from different side boundaries are marked with different colours).